TISSUE ENGINEERING: Part A
Volume 15, Number 8, 2009

DOI: 10.1089/ten.tea.2008.0382

Original Article

Solute Transport in Cyclically Deformed Porous Tissue Scaffolds with Controlled Pore Cross-Sectional Geometries

Jorn Op Den Buijs, M.Sc.,[1] Lichun Lu, Ph.D.,[2] Steven M. Jorgensen, B.Sc.,[1]
Dan Dragomir-Daescu, Ph.D.,[3] Michael J. Yaszemski, M.D., Ph.D.,[2] and Erik L. Ritman, M.D., Ph.D.[1]

The objective of this study was to investigate the influence of pore geometry on the transport rate and depth after repetitive mechanical deformation of porous scaffolds for tissue engineering applications. Flexible cubic imaging phantoms with pores in the shape of a circular cylinder, elliptic cylinder, and spheroid were fabricated from a biodegradable polymer blend using a combined 3D printing and injection molding technique. The specimens were immersed in fluid and loaded with a solution of a radiopaque solute. The solute distribution was quantified by recording 20 μm pixel-resolution images in an X-ray microimaging scanner at selected time points after intervals of dynamic straining with a mean strain of $8.6 \pm 1.6\%$ at 1.0 Hz. The results show that application of cyclic strain significantly increases the rate and depth of solute transport, as compared to diffusive transport alone, for all pore shapes. In addition, pore shape, pore size, and the orientation of the pore cross-sectional asymmetry with respect to the direction of strain greatly influence solute transport. Thus, pore geometry can be tailored to increase transport rates and depths in cyclically deformed scaffolds, which is of utmost importance when thick, metabolically functional tissues are to be engineered.

Introduction

Tissue engineering frequently utilizes porous scaffolds. One use of scaffolds is to cultivate cells on the scaffold *in vitro* and subsequently implant the construct *in vivo*. Before implantation, bioreactors may be used to perfuse the engineered tissue to provide cells beyond the diffusion distance with the essential oxygen (O_2) and nutrients, and to remove toxic waste as a result of cell metabolism and scaffold degradation.[1,2] However, lack of proper mass transport after application *in vivo* may result in cell density decreasing from the periphery to the center of the construct due to chemotaxis and/or necrosis of cells beyond the diffusion distance,[3–5] which may ultimately lead to functional failure of the implant. An alternative approach is to directly implant acellular scaffolds, coated or embedded with bioactive molecules (e.g., growth factors), to induce *in vivo* ingrowth of vascularized tissue.[6] Still, the infiltration of cells and microvessels into deep layers of the scaffold depends on adequate rate of solute transport. Therefore, approaches are required to supply the scaffold with nutrients and O_2 between the time of implantation and the establishment of blood supply.[3,7]

Under static conditions, nutrient transfer is governed by diffusion, that is, transport driven by a concentration gradient. However, diffusive transport is relatively slow (e.g., Fermor *et al.*[8] reported diffusivities of approximately 2.5×10^{-7} cm^2 s^{-1} for uncharged dextrans in the surface zone of cartilage) and generally accounts for supplying cells at a depth of only a few hundred micrometers from the surface within a reasonable time.[9] In particular, for articular cartilage, which lacks a vascular bed, the notion arose that a pumping action due to joint mobility could contribute to cartilage nutrition.[10] This was later supported by absorption/desorption measurements during repetitive loading of cartilage explants.[11,12] Tissue engineers took advantage of this idea by showing that application of dynamic deformational loading to cartilage constructs promoted tissue ingrowth

[1]Physiological Imaging Research Laboratory, Department of Physiology and Biomedical Engineering, Mayo Clinic College of Medicine, Rochester, Minnesota.
[2]Tissue Engineering and Biomaterials Laboratory, Department of Physiology and Biomedical Engineering and Department of Orthopedic Surgery, Mayo Clinic College of Medicine, Rochester, Minnesota.
[3]Division of Engineering and Department of Physiology and Biomedical Engineering, Mayo Clinic College of Medicine, Rochester, Minnesota.
This work was performed at Mayo Clinic, Rochester, Minnesota.

in vitro and improved their mechanical properties.[13,14] Because most tissues experience a certain degree of repetitive mechanical strain, the concept of mechanical loading has also been applied to improve *in vitro* engineered cardiovascular constructs,[15,16] heart valves,[17] smooth muscle tissue,[18] bone,[19] and fibroblast scaffolds for tendon and ligament engineering.[20] Although other factors such as fluid shear and increased protein expressions play a role in the observed improvements over static controls,[18,19] enhanced nutrient transport and waste removal due to rhythmic deformation of the porous scaffolds likely contributed.[21]

Measurements of transport rates through porous scaffolds have been previously made by applying a pressure gradient over the scaffold and quantifying the flow through the scaffold,[3,22] or by sampling the concentration in the surrounding fluid reservoir.[23] However, these techniques are unable to measure the solute distribution inside the specimens, which ultimately determines where cells can or cannot survive. Confocal microscopy has been used to quantify transport of fluorescent solutes in cartilage,[12] but the limited penetration depth of optical methods requires thin, translucent specimens (<1 mm). To overcome these limitations, an X-ray microimaging technique was developed to quantify the movement of solutes through pores in polymeric scaffolds (>5 mm) while they were repeatedly squeezed.[24] X-ray microimaging and micro-CT have become widely used imaging modalities in biomedical research,[25] enabling imaging within opaque specimens at micrometer spatial resolution without the need to destroy the sample.[26] Micro-CT has been applied to track bone ingrowth into scaffolds *in vitro*[27] and *in vivo*.[5,28,29] The accurate scaffold pore geometry as obtained with micro-CT can also be used to quantitatively analyze pore interconnectivity,[30] or, in combination with computational fluid dynamics, to predict fluid stream lines upon (hypothetical) perfusion of the scaffold.[31–33] Moreover, precise quantitative information about the local concentration of an X-ray absorbing contrast agent (for instance as a surrogate for nonradiopaque nutritional solutes or metabolic waste) can be obtained with micro-CT.[34]

The specific aim of this study was to quantify solute transport induced by mechanical compression in cubic imaging phantoms with a range of selected pore geometries, representing simplified tissue engineering scaffolds. Deformable, biodegradable specimens with programmable pore cross-sectional shapes were fabricated using a 3D printing and injection molding technique. The imaging phantoms were immersed in fluid, loaded with an X-ray absorbing dye, and mechanically compressed inside a custom-made X-ray microscanner. The recorded X-ray images were quantitatively analyzed as to the rate and spatial distribution of solute transport in the porous phantoms.

Materials and Methods

Scaffold material

Polypropylene fumarate (PPF) with a number-average molecular weight (M_n) of 3460 g mol^{-1} and a weight-average molecular weight (M_w) of 7910 g mol^{-1} and polycaprolactone fumarate (PCLF) with an M_n of 3520 g mol^{-1} and an M_w of 6050 g mol^{-1} were used to prepare PPF/PCLF blends. PPF and PCLF were synthesized as described earlier.[35] The PCLF sample used here was synthesized using α,ω-telechelic PCL diol with a nominal M_n of 530 g mol^{-1} and fumaryl chloride in the presence of potassium carbonate.[36]

Both PPF and PCLF are biodegradable, crosslinkable, and biocompatible.[37–39] Crosslinked PPF and PCLF have distinct characteristics because of different density of crosslinkable segment on the polymer backbone. Crosslinked PPF is a stiff material with an average tensile modulus $E = 1.3$ GPa, while crosslinked PCLF is a flexible material with $E = 2.1$ MPa. Material properties, particularly mechanical properties, can be modulated through varying the composition of PPF in PPF/PCLF blends.[40] In the present study, one PPF/PCLF blend with PPF weight composition of 25% and PCLF composition of 75% was prepared by first dissolving PPF and PCLF sufficiently in a co-solvent methylene chloride (CH_2Cl_2) and then evaporating the solvent in a vacuum oven.

Scaffold fabrication

A previously described method[41] was used to manufacture image phantoms with programmable pore structures, as simplified models of tissue scaffolds. Computer-aided design (CAD) models were created using SolidWorks (SolidWorks Corp., Concord, MA), meshed into stereolithography (STL) files, and converted to 2D sliced data files with a thickness of 76 μm using the ModelWorks software (Solidscape Corp., Merrimack, NH). The 3D phase-change ink jet printer, PatternMaster, was used to create 3D injection molds by printing the 2D sliced data files layer by layer with a build material (polystyrene) and a support material (wax). After printing, the polystyrene was dissolved by immersing the printed cubes into acetone for 30 min. to leave wax molds. Subsequently, the wax molds were put into a Teflon holder, and PPF/PCLF polymerizing mixture was injected under vacuum. The PPF/PCLF polymer blend was then crosslinked by free-radical polymerization with benzoyl peroxide, dimethyl toluidine, 1-vinyl-2-pyrrolidinone, and methylene chloride as free-radical initiator, accelerator, crosslinker, and diluent, respectively. About 100 μL of initiator solution (50 mg of benzoyl peroxide in 250 μL of 1-vinyl-2-pyrrolidinone) and 40 μL of accelerator solution (20 μL of dimethyl toluidine in 980 μL of methylene chloride) were added and mixed. To facilitate crosslinking, specimens were put into the oven at 40°C for 1 h. After crosslinking was completed, the specimens were detached from the Teflon holder and the wax was dissolved in a cleaner solution (BIOACT VS-O; Petroferm, Inc., Fernandina Beach, FL) at 40–60°C for 1 h. Finally, the specimens were dried completely at ambient temperature.

Scaffold and pore geometry

Cubic injection molds (5.0 mm on a side) were printed, such that imaging phantoms with pores consisting of a single channel through the middle of the specimen could be generated. Pores with the following cross-sectional and longitudinal shapes were designed: circular cylinder, elliptic cylinder, and spheroid. Five specimens were generated for each shape. After crosslinking of the polymer in the mold, the final dimensions were slightly altered compared to the original design, presumably due to shrinkage of the polymer. To accurately determine the dimensions of the finally created phantoms, they were scanned in air (no fluid and/or contrast

agent present) with micro-CT at 20 μm voxel resolution using a custom-made X-ray imaging system.[26] No swelling or shrinking of the specimens after immersion in fluid was observed.

Experimental setup

Experiments were carried out at room temperature. The imaging phantoms were glued to the bottom of a fluid reservoir placed underneath the loading platen of a custom-made compression device. The setup was mounted inside a custom-made high-resolution X-ray imager (Fig. 1). The fluid reservoir was filled with 99.5% glycerol with a viscosity of ~1.0 Pa s, which closely matched the viscosity of the iodine-based contrast medium, decreasing gravitational settling of the tracer and therefore enabling X-ray exposure times of several seconds. A solution of the radiopaque contrast agent sodium iodide (NaI; Sigma-Aldrich, Inc., St. Louis, MO) in glycerol (25.8 mg mL^{-1} I^-) was rendered visible to the eye with a drop of blue food coloring. A needle syringe with blunt tip was used to infuse the contrast agent into the specimen's pore until it was completely filled, and the syringe was then slowly withdrawn from the fluid reservoir. After this infusion, convective transport was induced by cycles of compression and release applied to the top face of the specimen. The compression amplitude was measured using X-ray projection images of the specimen in the uncompressed state and in the maximally compressed state. The percentage of compression was calculated from the images as:

$$\left|\frac{H-H_0}{H_0}\right| \cdot 100\%, \tag{1}$$

where H_0 and H are the phantom height at rest and upon maximal compression, respectively. The compression rate was set at 1.0 Hz.

Projection X-ray imaging protocol

The specimens were imaged in a custom-made high-resolution X-ray system consisting of a spectroscopy X-ray source with a molybdenum anode and zirconium foil filter so that the K_α emission radiation (17.5 keV) photons predominate in the emitted X-ray spectrum. The specimen's X-ray image was converted into a light image in a Terbium-doped fiber optic glass plate coupled to a charge-coupled device (CCD) array. The CCD image, consisting of 1340×1300 pixels, was then recorded. The pixel size in the X-ray image was 20 μm, so that the spatial resolution is approximately 40 μm and, hence, pore diameter differences of ~500 μm are readily resolved. Specimens were placed at 5.5 cm from the detector, and the distance between X-ray source and detector was 98.5 cm. X-ray exposure time was 5.0 s, and a scintillator decay time of 0.5 s was allowed for. The compression device was switched on and off from outside the lead-lined scanner-housing. Images of the fluid-filled specimens were recorded before and right after injection of the contrast agent. Further, during passive experiments (compression turned off), images were recorded after 1, 3, 5, and 10 min. During active experiments (compression turned on) images were recorded after 5, 10, … , 50, 75, 100, 150, 200, and 300 compression cycles, by temporarily pausing the cyclic compression during the imaging time of 5.7 s, with the specimen in the uncompressed state. The total imaging time was less than 2 min per experiment, during which passive removal may have contributed to transport. However, based on the measurements during passive removal, it is expected that passive removal contributed less than 10% to the total solute transport during the time required for imaging.

Image analysis

The transmitted X-ray intensity I, at each pixel, is given by:

$$I = I_0 \exp\left(-\sum_i \mu_i x_i\right), \tag{2}$$

where I_0 is the incident X-ray intensity, μ_i is the linear attenuation coefficient of material i, and x_i is the thickness of material i along the X-ray beam illuminating the pixel after passing through the imaging phantom. The total X-ray

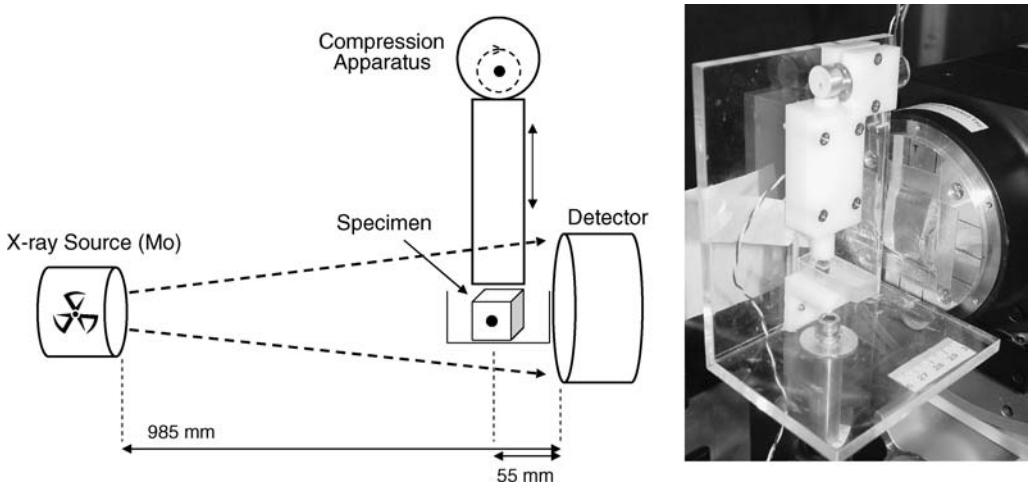

FIG. 1. Schematic diagram (left) and photograph (right) of the experimental setup. The specimen is placed inside a fluid reservoir underneath a compression device. A molybdenum X-ray source is used to generate projection images of the specimen pore injected with X-ray contrast agent.

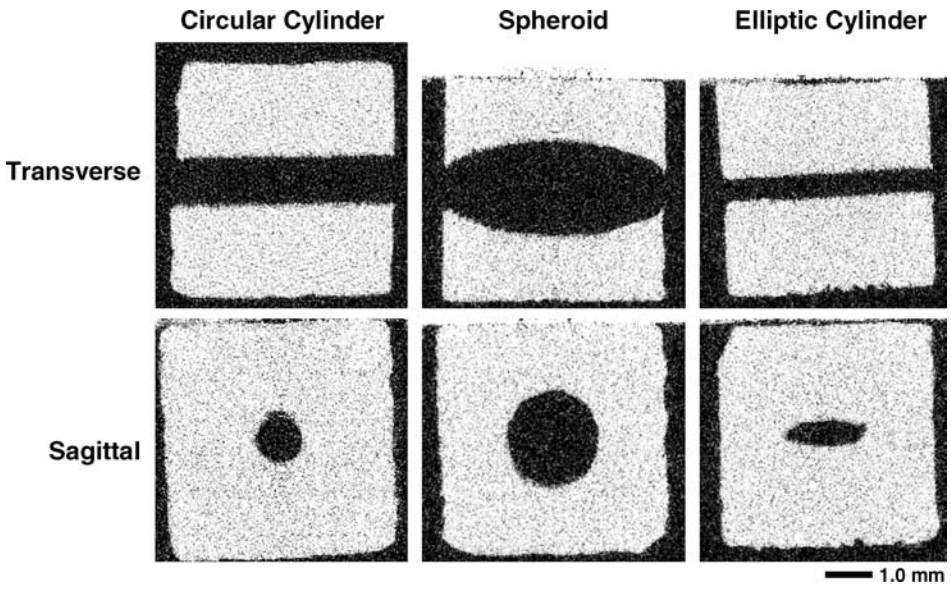

FIG. 2. Representative micro-CT images (20 μm voxel size) of the specimens with pores in the form of a circular cylinder (1.5 mm), spheroid, and elliptic cylinder. White is scaffold material; black is air.

attenuation $\sum_i \mu_i x_i$ is mainly due to the iodine in the channel, the polymer material which the specimen is made of, and the glycerol in the surrounding fluid reservoir. The attenuation due to iodine in the pore was then calculated by subtracting the attenuation before contrast agent injection from the attenuation measured with iodine present in the pore. The average attenuation due to iodine was obtained by averaging the attenuation over the entire pore volume. Under the assumption that the attenuation coefficient of the iodine is linearly proportional to the iodine concentration (because the pore dimension remains unchanged in between compressions), the average iodine concentration in the channel was calculated as a fraction of the average iodine concentration calculated immediately after injection.

Statistical analysis

To statistically compare the results of the image analysis, the remaining fraction of iodine (as measured after 300 s of passive removal or after 300 compression cycles at 1.0 Hz) was evaluated with one-way analysis of variance (ANOVA). This fraction was calculated in specimens with different channel shapes and compared with the 0.5 mm circular cylindrical channel by a Tukey-Kramer honestly significant difference test ($^{\#}p < 0.05$). For each channel shape, the effect of passive and deformation-induced transport was compared by a two-tailed *t*-test ($^{*}p < 0.05$).

Results

Scaffold pore geometry

Representative micro-CT images (20 μm voxel resolution) of the specimens are shown in Figure 2. These images were used to quantify the actual (as distinct from the programmed) pore dimensions (Table 1). The average side dimension of all specimens was 4.50 ± 0.18 mm.

Scaffold compression

Figure 3 shows representative projection X-ray images of the scaffold in the uncompressed state compared to the compressed state. It can be noted that the spheroid is mainly compressed in the middle, whereas its openings to the reservoir are slightly narrowed during compression. From the front view of the specimen with elliptic channel, it can be

Table 1. Channel Dimensions of Initial Computer-Aided Design (CAD) Models and Actual Specimens After Manufacturing as Measured with Micro-CT

	Circular cylinder channel diameter (mm)			
CAD design	0.5	1.0	1.5	2.0
Micro-CT measured	0.37 ± 0.030	0.94 ± 0.026	1.38 ± 0.048	1.89 ± 0.028
	Elliptic cylinder channel diameter (mm)		*Spheroid channel diameter (mm)*	
	Minor axis	*Major axis*	*At openings*	*Maximum*
CAD design	0.6	2.0	0.55	2.0
Micro-CT measured	0.54 ± 0.043	1.75 ± 0.043	0.73 ± 0.076	1.89 ± 0.017

For the circular cylinder, scaffolds with four different diameters were generated. For the elliptic cylinder, the minor and major axis dimensions of the channel cross section are given. For the spheroid, the diameter at the channel openings, and the maximum diameter in the middle are given. All specimens were cubic with an average side dimension of 4.50 ± 0.18 mm.

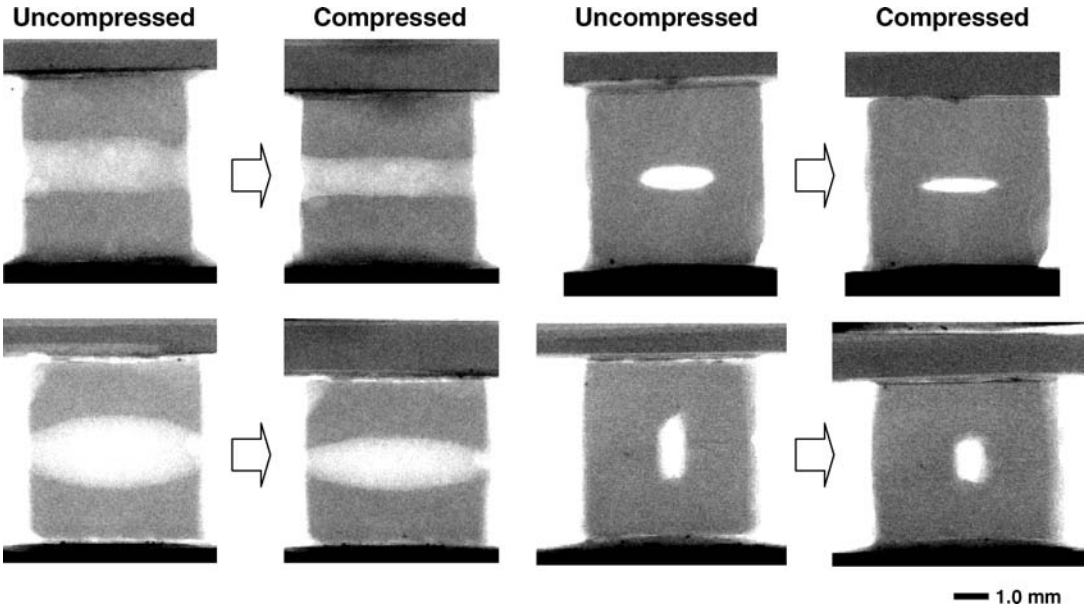

FIG. 3. Projection X-ray images of the uncompressed specimen and the specimen at maximal level of compression. Side views are shown for the 1.5-mm-diameter circular cylinder (top left) and spheroid channel (bottom left). The elliptical channel is shown from the front with the compression perpendicular to (top right) and in parallel with (bottom right) the major axis of the elliptical cross section.

observed that when the major axis of the elliptic cross-section is perpendicular to the direction of compression, it is highly deformed ($65 \pm 5\%$ compression along the semi-minor axis, see Table 2). In contrast, the elliptic cross section becomes more circular when its major axis is in the same direction as the compression.

On average, the percentage of scaffold compression was $8.6 \pm 1.6\%$ of the original specimen height and not significantly different among the different scaffolds as tested by ANOVA. Thus, the scaffold compression amplitude did not depend on the pore shape. For the circular cylindrical channels with different diameters, the percentage of compression of the channel decreased with increasing diameter (Table 2).

Solute transport

Projection X-ray images show the removal of the iodine from the scaffold channel, as caused by passive removal or removal induced by consecutive cycles of deformation of the scaffold (Fig. 4). The images demonstrate that after 300 s of passive removal without compression, most of the iodine is still present in the channels. Particularly in the case of the circular cylinder, it can be seen that a portion of the contrast agent is slowly removed, in part due to gravity-induced natural convection as a result of the slight difference in density between the fluid containing NaI and the fluid without the contrast agent. In addition, it can be observed that after 300 cycles of compression at 1.0 Hz (i.e., corresponding to 300 s), most of the contrast agent is removed from the phantom with the elliptical cross section pore. In contrast, only approximately 50% of iodine is removed from the circular pore, and most of the dye remains inside the spheroidal pore.

The average iodine concentration inside the channel was calculated relative to the iodine concentration right after injection. This quantitative analysis shows the effect of the pore shape on the removal rate during compression cycles (Fig. 5). The remaining fraction of iodine in the channel after 300 s is shown (Fig. 6A) for all channel shapes as a result of both passive and deformation-induced removal. A statistically significant difference between passive and strain-induced removal was found for all pore shapes. The remaining fraction of iodine 300 s after passive removal was statistically

Table 2. Percentage Compression of the Channels of the Specimens, Measured Along the Vertical Direction

Channel geometry	*CAD diameter (mm)*	*Channel compression (%)*
Circular	0.5	45 ± 6
	1.0	48 ± 4
	1.5	33 ± 3[a]
	2.0	26 ± 1[a]
Elliptic (strain parallel to semi-minor axis)	0.6	65 ± 5[a]
Elliptic (strain parallel to semi-major axis)	2.0	18 ± 1[a]
Spheroid	2.0	17 ± 1[a]

[a]Significantly different from 0.5 mm ($p < 0.05$).

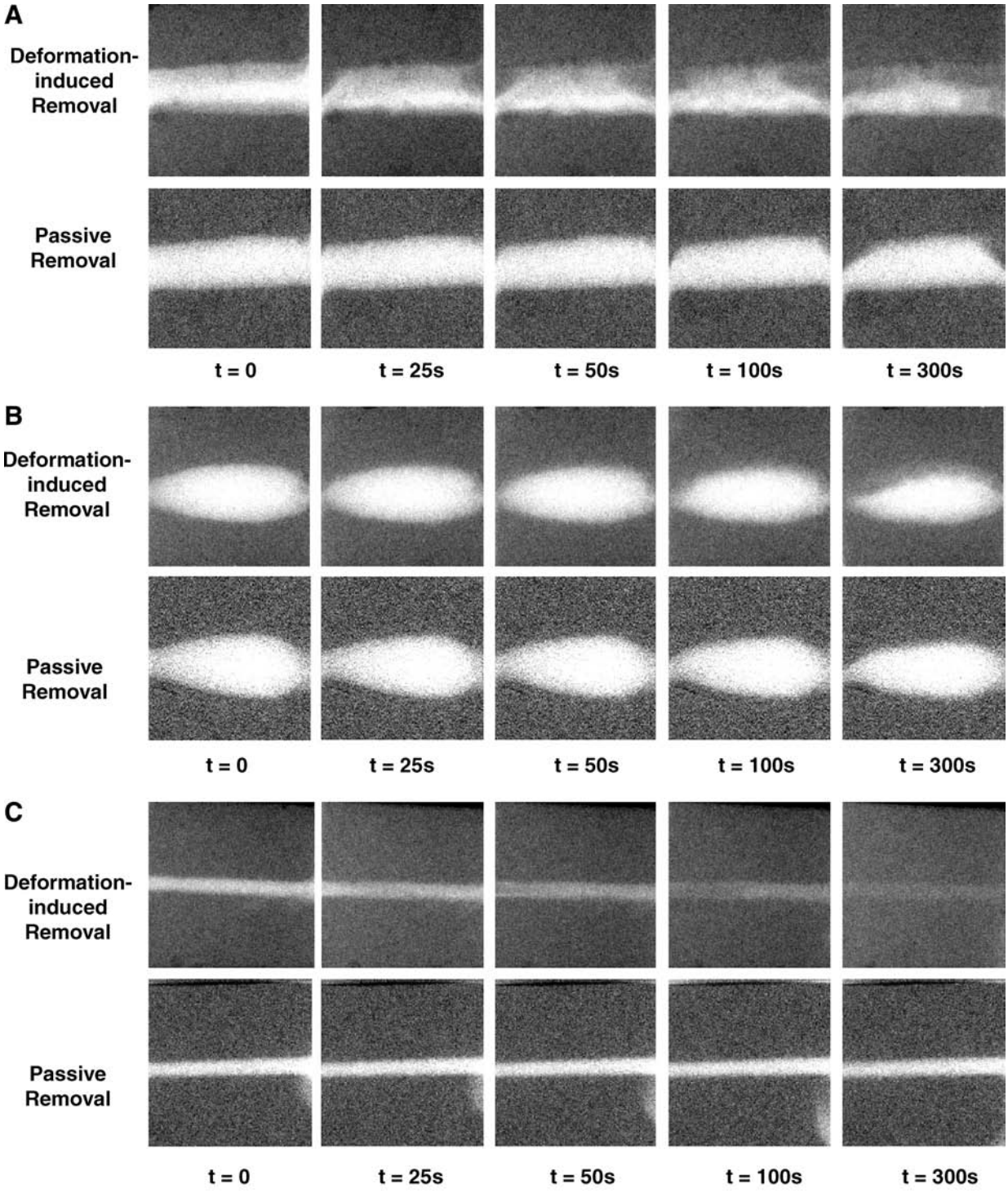

FIG. 4. Consecutive projection X-ray images taken during compression-induced and passive removal of NaI from the specimen channels. Compression was performed at 1.0 Hz, such that 300 s correspond to 300 compressions. (**A**) Circular pore (1.5 mm diameter). (**B**) Spheroid pore. (**C**) Elliptic pore.

different from the 0.5 mm circular only for the 2.0 mm pore, likely due to increased gravitational settling. After 300 s of strain-induced removal, the remaining fraction of iodine was significantly different from the 0.5 mm pore for the 1.5 mm circular pore, the spheroid pore, and the elliptic pore (in both directions of compression). With the exception of the 2.0 mm circular pore, the remaining fraction of iodine in the channel after 300 s correlated well with the channel compression (Fig. 6B). Upon exclusion of the 2.0 mm circular pore, linear regression yielded a relationship of $y = -0.00131x + 0.9735$, with $R^2 = 0.9803$. Increased gravitational settling in the 2.0 mm pore likely caused the increased rate of solute transport as would have been expected based on the percentage of channel compression.

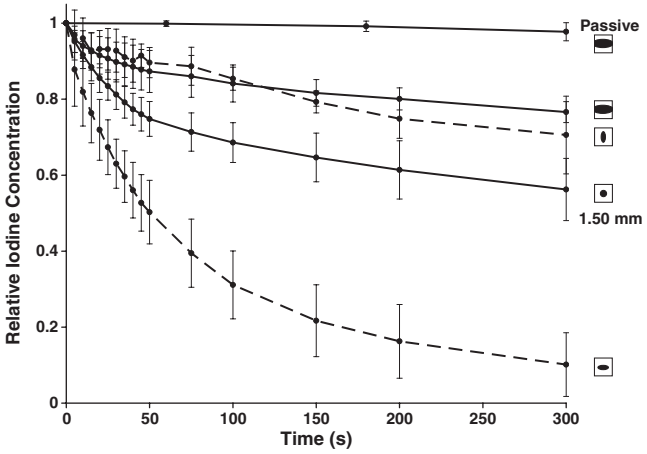

FIG. 5. Relative iodine concentration in the specimen channel upon deformation-induced removal for the spheroid channel, 1.50 mm circular cylindrical channel, and elliptical channel. Data represent means ± SD for $n = 5$.

To illustrate the spatial distribution of solute transport in the different scaffold types, images recorded right after iodine injection were subtracted from images recorded after 300 compression cycles (Fig. 7). White areas in these images represent spots where most of the contrast agent has been removed after 5 min of cyclic deformation.

Discussion

Dynamic transport of an X-ray tracer inside cyclically deformed imaging phantoms with designed pore geometries, mimicking porous tissue scaffolds, was imaged using an X-ray microimaging technique. The main finding of this study was that solute transport rates and depths can be significantly influenced by the shape of the pore, its dimension, and the orientation of its cross section with respect to the direction of the cyclic strain.

Increasing the diameter of the circular cylindrical channels from 0.5 to 1.5 mm slightly decreased the deformation-induced solute transport rates, which correlated with the decreased percentage of channel compression of the 1.5 mm channel. The increased passive removal in the 2.0 mm diameter channel as compared to the 0.5 mm channel most likely compensated for this effect. The spheroidal channel showed the slowest transport rates during both passive removal and compression-induced removal. This may be attributed to its relatively large volume compared to its smaller cross section exposed to the surrounding fluid reservoir. The elliptic cylinder with its major axis perpendicular to the direction of compression was highly collapsible and therefore yielded a high solute transport rate under cyclic compression. In contrast, when its major axis was in parallel with the direction of compression, solute transport was significantly reduced, indicating the strong influence of pore orientation compared to direction of strain.

Limited mass transport currently hinders the development of thick tissue-engineered implants, and O_2 is arguably the most important metabolic substrate to be transported to the cells inside the scaffolds to maintain normal cell function. Sensitivity to hypoxia varies among cells: 40% of cells cultured under hypoxia do not survive after ~5 days for endothelial cells,[42] after ~12 h for cardiomyocytes,[43] and after only ~2 h for preadipocytes[44] (cells of interest in adipose tissue engineering). To sustain viable (not necessarily functional) cells inside the scaffolds, O_2 transport rate must match rate of O_2 consumption, which is of the order of 1–10 nmol O_2 min^{-1} $(10^6$ cells$)^{-1}$ for a range of cell types.[45,46] The present results indicate that the time to reach 37% of the initial iodine (as a surrogate for O_2) concentration for the elliptic pore compressed along its semi-minor axis was approximately 1 min (Fig. 5), yielding an average transport rate of 0.63 min^{-1}. Given an arterial plasma O_2 concentration of 130 μmol L^{-1} and an average O_2 consumption of 5 nmol O_2 min^{-1} $(10^6$ cells$)^{-1}$, an estimate for the sustainable cell density in the scaffold can then be calculated:

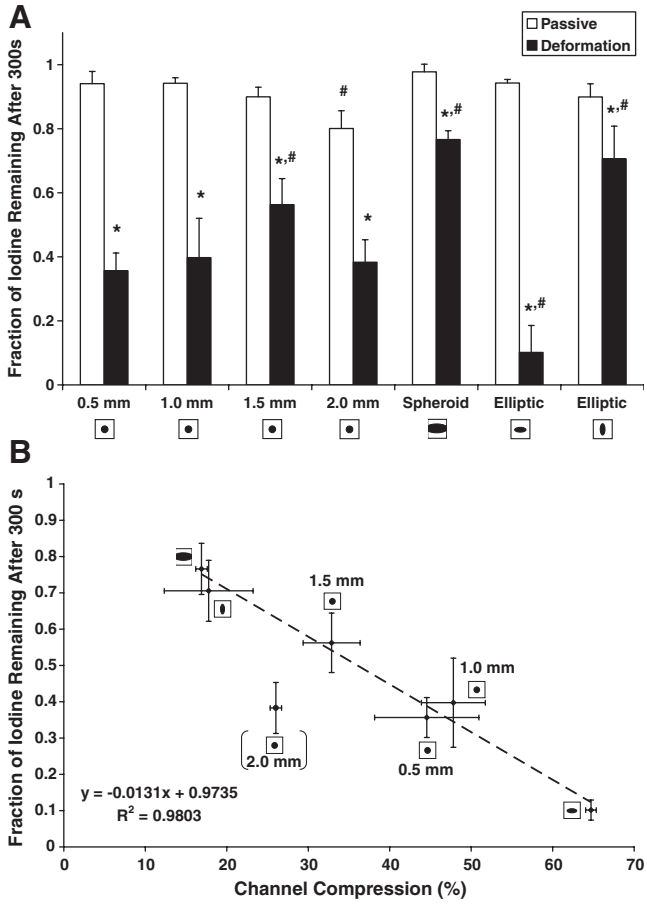

FIG. 6. (**A**) Fraction of remaining iodine concentration after 300 s of passive transport (white bars) or deformation-induced transport (black bars). Data represent means ± SD for $n = 5$. *Significantly different compared to passive removal ($p < 0.05$). #Significantly different compared to 0.5-mm-diameter channel ($p < 0.05$). (**B**) Correlation between channel compression and remaining fraction of iodine after 300 s of compressions for the different channel shapes. Linear regression yielded a significant relationship ($y = -0.0131x + 0.9735$, $R^2 = 0.9803$). Note that the 2.0 mm circular channel was excluded from the regression.

$$\frac{130 \cdot 10^{-6}\,\text{mol}\,\text{L}^{-1} \cdot 0.63\,\text{min}^{-1}}{5 \cdot 10^{-9}\,\text{mol}\,\text{min}^{-1}\,(10^6\,\text{cells})^{-1}} = 1.6 \cdot 10^7\,\text{cells}\,\text{ml}^{-1} \quad (3)$$

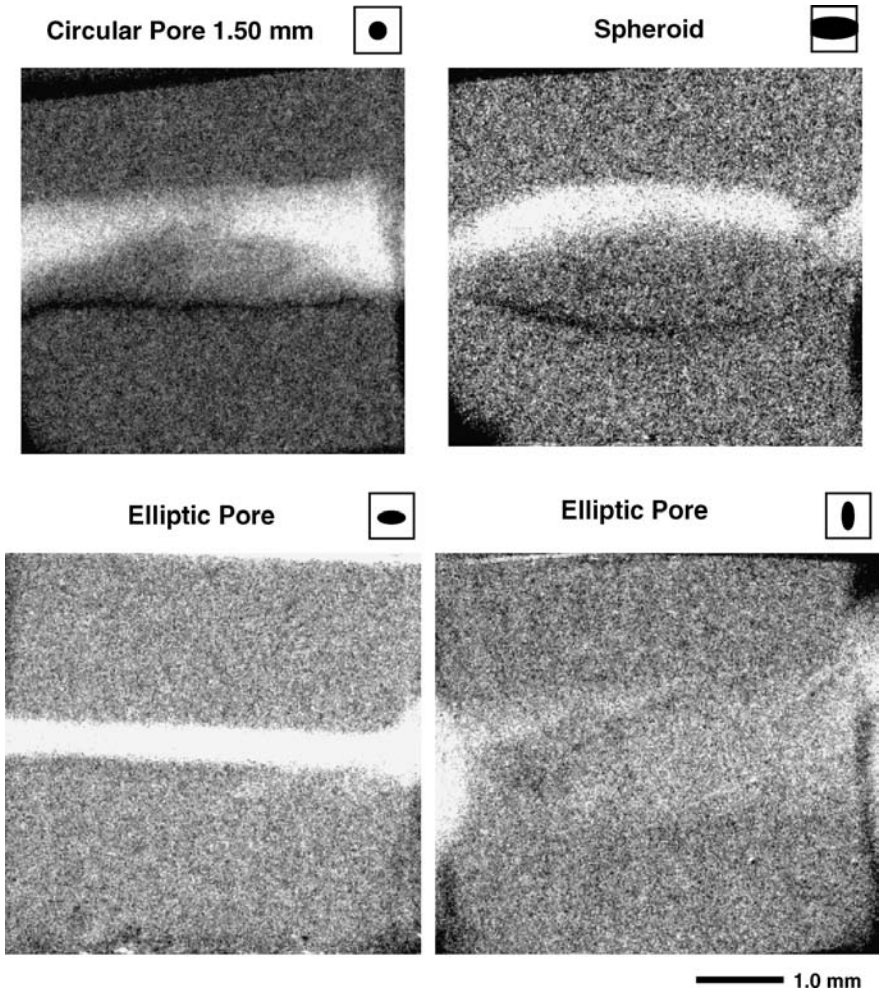

FIG. 7. Grayscale images of the measured intensities right after injection, subtracted from the measured intensity after 300 compression cycles. White pixels mean that contrast agent was completely removed at this position. Difference images are shown for the 1.5 mm circular cylinder pore (top left), the spheroid (top right), and the elliptic pore in both directions (bottom).

This is still one to two orders of magnitude lower than cell densities in most human vascularized tissues; however, cyclic strain may induce sufficient temporary convective nutrient transport to maintain viable cells, while ingrowth of microvessels proceeds after implantation of the scaffold. Even more, although solute convection dominates transport in these experiments, the diffusion coefficient of O_2 in aqueous solution is likely higher as compared to NaI in glycerol due to lower solvent viscosity and lower molecular weight (32 g mol^{-1} for O_2 vs. 149.9 g mol^{-1} for NaI), which could increase the sustainable cell density.

Increased convective transport properties of the scaffold will trade off with its ability to provide temporary mechanical support at the site of implantation. Pores with elliptical cross-section oriented with the semi-minor axis along the strain direction may yield high transport rates, but the effective scaffold stiffness will be lower than when a pore with, for example, a circular cross-section is used. The need for scaffolds with an adequate balance between mechanical and mass transport properties thus requires the ability to precisely control the scaffold topology.[47] In contrast to commonly used methods to create porous sponges of scaffold materials (e.g., particulate leaching[48,49] or gas foaming[50]), the solid freeform technique used in this study allows the fabrication of scaffolds with programmable pore labyrinths. Designer-scaffolds have more predictable mechanical properties, mass transport rates, and spatial distributions than do scaffolds generated with such traditional methods.

This study has several limitations. Pore diameters of the imaging phantoms ranged from 370 μm to 1.91 mm, although the current results may also be relevant for pores with smaller dimensions. Optimal pore sizes for tissue engineering scaffolds have been suggested to lie between 100 and 500 μm, depending on the cell type.[51] It should be noted that these smaller dimensions are largely based on studies using scaffolds fabricated with salt-leaching techniques. In contrast, bone ingrowth has been successfully demonstrated in scaffolds with pore sizes greater than 1.0 mm as manufactured by SFF[52] or a combination of phase-inversion and particulate extraction.[53]

Scaffolds with simple pores comprised of single straight channels with various shapes were used, whereas more realistic scaffolds would have pore labyrinths comprised of interconnected channels in three dimensions. Using the described scaffold fabrication technique, it is possible to manufacture more complex pore structures. A qualitative demonstration of the techniques described in this paper, applied to a simple pore network of 1.0 mm diameter interconnected circular channels in a single plane, is shown in Figure 8. Imaging the contrast agent distribution after cyclic deformation in three dimensions would require a tomographic method such as micro-CT. The relatively long

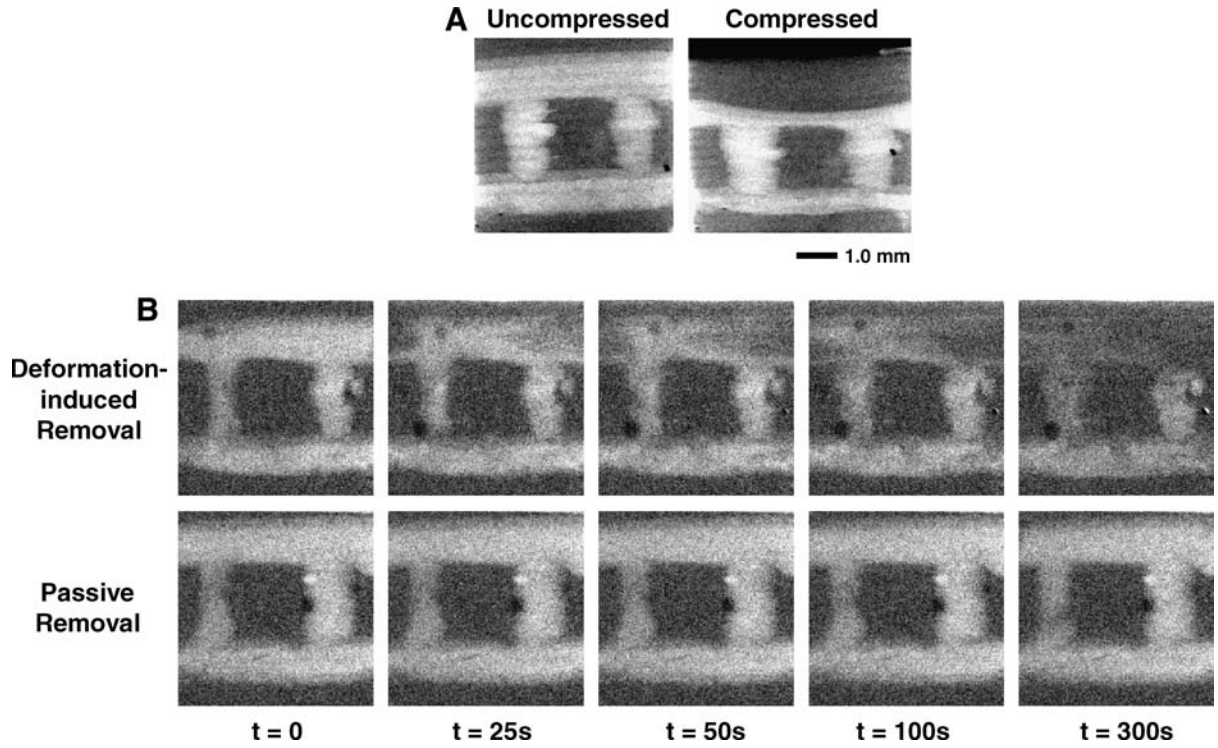

FIG. 8. (**A**) Projection X-ray images of an imaging phantom with simple 2D pore network in the uncompressed state and at maximal level of compression (16.6% of the original height). (**B**) Consecutive projection X-ray images taken during compression-induced and passive removal of NaI from the phantom channels.

acquisition times associated with micro-CT (of the order of minutes) could introduce motion artifacts due to diffusion and/or gravitational settling of the X-ray tracer. Recent developments in high-speed X-ray microimaging may be sufficiently fast to accomplish CT scans in seconds.[54] Another potential solution to this problem may be the recently developed cryostatic micro-CT method[55] in which specimens are snap-frozen during the solute transport process and scanned while frozen.

In vivo, many tissues are subjected to specific mechanical cues. For instance, bone and cartilage undergo dynamic compression during joint mobility, whereas tendons, muscle, and blood vessel walls can experience large dynamic tensile strains. Although the effects of cyclic stretch on solute transport were not investigated in the current study, pore geometry affects solute transport most likely in a similar way under cyclic stretch as it does during cyclic compression: highly deforming pore geometries, such as the elliptic cylinder with its semi-minor axis in the strain direction, will yield high solute transport rates. Further studies are needed to confirm this prediction.

The X-ray contrast agent NaI is based on the high atomic weight of the element iodine. In addition, the concentration of NaI was higher than most physiological substances to ensure a reasonable signal-to-noise ratio in the images. This resulted in gravitation-induced convection of the tracer, explaining the somewhat higher passive removal rate as would have been expected based on diffusional transport alone. To reduce the influence of gravitational settling, glycerol with a viscosity of $\sim$1.0 Pa s (as compared to 1.0 mPa s for water and 1.31 mPa s for human blood plasma[56]) was used as the solvent. This will have likely decreased the diffusion of the iodine because the diffusion coefficient is inversely proportional to viscosity according to the Stokes-Einstein equation.[57] The impact of viscosity on the convective part of the compression-induced solute transport is less clear. Increased viscosity increases the resistance to flow, which could potentially inhibit convective transport; however, increased resistance simultaneously increases the pressure inside the channel because the compression device now has to deliver a slightly higher force to achieve the same amount of deformation. It could well be that these two mechanisms cancel each other out to a great extent.

Conclusion

The results demonstrate that shape, size, and orientation of pores in a tissue scaffold have great effects on solute transport during cyclic mechanical deformation. This has implications for the design of the pore system of thick, deformable implants in which enhanced solute transport rates are desired to facilitate tissue ingrowth. Additionally, pore geometry may be adjusted to achieve ideal release constants in deformable porous drug delivery systems.

Acknowledgments

This work was in part supported by Mayo Foundation and NIH Grant EB000305. The authors thank Dr. Kee-Won Lee for scaffold manufacturing and Mr. James A. Gruetzmacher for polymer synthesis.

Disclosure Statement

No competing financial interests exist.

References

1. Mygind, T., Stiehler, M., Baatrup, A., Li, H., Zou, X., Flyvbjerg, A., Kassem, M., and Bunger, C. Mesenchymal stem cell ingrowth and differentiation on coralline hydroxyapatite scaffolds. Biomaterials **28,** 1036, 2007.
2. Carrier, R.L., Rupnick, M., Langer, R., Schoen, F.J., Freed, L.E., and Vunjak-Novakovic, G. Perfusion improves tissue architecture of engineered cardiac muscle. Tissue Eng **8,** 175, 2002.
3. Karande, T.S., Ong, J.L., and Agrawal, C.M. Diffusion in musculoskeletal tissue engineering scaffolds: design issues related to porosity, permeability, architecture, and nutrient mixing. Ann Biomed Eng **32,** 1728, 2004.
4. Ramrattan, N.N., Heijkants, R.G., van Tienen, T.G., Schouten, A.J., Veth, R.P., and Buma, P. Assessment of tissue ingrowth rates in polyurethane scaffolds for tissue engineering. Tissue Eng **11,** 1212, 2005.
5. Silva, M.M., Cyster, L.A., Barry, J.J., Yang, X.B., Oreffo, R.O., Grant, D.M., Scotchford, C.A., Howdle, S.M., Shakesheff, K.M., and Rose, F.R. The effect of anisotropic architecture on cell and tissue infiltration into tissue engineering scaffolds. Biomaterials **27,** 5909, 2006.
6. Yamamoto, M., Tabata, Y., Kawasaki, H., and Ikada, Y. Promotion of fibrovascular tissue ingrowth into porous sponges by basic fibroblast growth factor. J Mater Sci Mater Med **11,** 213, 2000.
7. Volkmer, E., Drosse, I., Otto, S., Stangelmayer, A., Stengele, M., Kallukalam, B.C., Mutschler, W., and Schieker, M. Hypoxia in static and dynamic 3D culture systems for tissue engineering of bone. Tissue Eng Part A **14,** 1331, 2008.
8. Fermor, B., Christensen, S.E., Youn, I., Cernanec, J.M., Davies, C.M., and Weinberg, J.B. Oxygen, nitric oxide and articular cartilage. Eur Cell Mater **13,** 56; discussion 65, 2007.
9. Brown, D.A., MacLellan, W.R., Laks, H., Dunn, J.C., Wu, B.M., and Beygui, R.E. Analysis of oxygen transport in a diffusion-limited model of engineered heart tissue. Biotechnol Bioeng **97,** 962, 2007.
10. Maroudas, A., Bullough, P., Swanson, S.A., and Freeman, M.A. The permeability of articular cartilage. J Bone Joint Surg Br **50,** 166, 1968.
11. O'Hara, B.P., Urban, J.P., and Maroudas, A. Influence of cyclic loading on the nutrition of articular cartilage. Ann Rheum Dis **49,** 536, 1990.
12. Evans, R.C., and Quinn, T.M. Solute convection in dynamically compressed cartilage. J Biomech **39,** 1048, 2006.
13. Mauck, R.L., Seyhan, S.L., Ateshian, G.A., and Hung, C.T. Influence of seeding density and dynamic deformational loading on the developing structure/function relationships of chondrocyte-seeded agarose hydrogels. Ann Biomed Eng **30,** 1046, 2002.
14. Hung, C.T., Mauck, R.L., Wang, C.C., Lima, E.G., and Ateshian, G.A. A paradigm for functional tissue engineering of articular cartilage via applied physiologic deformational loading. Ann Biomed Eng **32,** 35, 2004.
15. Boerboom, R.A., Rubbens, M.P., Driessen, N.J., Bouten, C.V., and Baaijens, F.P. Effect of strain magnitude on the tissue properties of engineered cardiovascular constructs. Ann Biomed Eng **36,** 244, 2008.
16. Akhyari, P., Fedak, P.W., Weisel, R.D., Lee, T.Y., Verma, S., Mickle, D.A., and Li, R.K. Mechanical stretch regimen enhances the formation of bioengineered autologous cardiac muscle grafts. Circulation **106,** I137-42, 2002.
17. Engelmayr, G.C., Jr., Rabkin, E., Sutherland, F.W., Schoen, F.J., Mayer, J.E., Jr., and Sacks, M.S. The independent role of cyclic flexure in the early *in vitro* development of an engineered heart valve tissue. Biomaterials **26,** 175, 2005.
18. Kim, B.S., Nikolovski, J., Bonadio, J., and Mooney, D.J. Cyclic mechanical strain regulates the development of engineered smooth muscle tissue. Nat Biotechnol **17,** 979, 1999.
19. Ignatius, A., Blessing, H., Liedert, A., Schmidt, C., Neidlinger-Wilke, C., Kaspar, D., Friemert, B., and Claes, L. Tissue engineering of bone: effects of mechanical strain on osteoblastic cells in type I collagen matrices. Biomaterials **26,** 311, 2005.
20. Joshi, S.D., and Webb, K. Variation of cyclic strain parameters regulates development of elastic modulus in fibroblast/substrate constructs. J Orthop Res **26,** 1105, 2008.
21. Mauck, R.L., Hung, C.T., and Ateshian, G.A. Modeling of neutral solute transport in a dynamically loaded porous permeable gel: implications for articular cartilage biosynthesis and tissue engineering. J Biomech Eng **125,** 602, 2003.
22. O'Brien, F.J., Harley, B.A., Waller, M.A., Yannas, I.V., Gibson, L.J., and Prendergast, P.J. The effect of pore size on permeability and cell attachment in collagen scaffolds for tissue engineering. Technol Health Care **15,** 3, 2007.
23. Lou, X., Munro, S., and Wang, S. Drug release characteristics of phase separation pHEMA sponge materials. Biomaterials **25,** 5071, 2004.
24. Op Den Buijs, J., Lee, K.W., Jorgensen, S.M., Wang, S., Yaszemski, M.J., and Ritman, E.L. High resolution X-ray imaging of dynamic solute transport in cyclically deformed porous tissue scaffolds. Proc SPIE, **6919,** 1A, 2008.
25. Ritman, E.L. Micro-computed tomography-current status and developments. Annu Rev Biomed Eng **6,** 185, 2004.
26. Jorgensen, S.M., Demirkaya, O., and Ritman, E.L. Three-dimensional imaging of vasculature and parenchyma in intact rodent organs with X-ray micro-CT. Am J Physiol **275,** H1103, 1998.
27. Hagenmuller, H., Hofmann, S., Kohler, T., Merkle, H.P., Kaplan, D.L., Vunjak-Novakovic, G., Muller, R., and Meinel, L. Non-invasive time-lapsed monitoring and quantification of engineered bone-like tissue. Ann Biomed Eng **35,** 1657, 2007.
28. Jones, A.C., Arns, C.H., Sheppard, A.P., Hutmacher, D.W., Milthorpe, B.K., and Knackstedt, M.A. Assessment of bone ingrowth into porous biomaterials using MICRO-CT. Biomaterials **28,** 2491, 2007.
29. van Lenthe, G.H., Hagenmuller, H., Bohner, M., Hollister, S.J., Meinel, L., and Muller, R. Nondestructive micro-computed tomography for biological imaging and quantification of scaffold-bone interaction *in vivo.* Biomaterials **28,** 2479, 2007.
30. Moore, M.J., Jabbari, E., Ritman, E.L., Lu, L., Currier, B.L., Windebank, A.J., and Yaszemski, M.J. Quantitative analysis of interconnectivity of porous biodegradable scaffolds with micro-computed tomography. J Biomed Mater Res A **71,** 258, 2004.
31. Sandino, C., Planell, J.A., and Lacroix, D. A finite element study of mechanical stimuli in scaffolds for bone tissue engineering. J Biomech **41,** 1005, 2008.
32. Jones, J.R., Poologasundarampillai, G., Atwood, R.C., Bernard, D., and Lee, P.D. Non-destructive quantitative 3D analysis for the optimisation of tissue scaffolds. Biomaterials **28,** 1404, 2007.
33. Cioffi, M., Boschetti, F., Raimondi, M.T., and Dubini, G. Modeling evaluation of the fluid-dynamic microenvironment in tissue-engineered constructs: a micro-CT based model. Biotechnol Bioeng **93,** 500, 2006.

34. Gossl, M., Beighley, P.E., Malyar, N.M., and Ritman, E.L. Role of vasa vasorum in transendothelial solute transport in the coronary vessel wall: a study with cryostatic micro-CT. Am J Physiol Heart Circ Physiol **287,** H2346, 2004.
35. Wang, S., Lu, L., and Yaszemski, M.J. Bone-tissue-engineering material poly(propylene fumarate): correlation between molecular weight, chain dimensions, and physical properties. Biomacromolecules **7,** 1976, 2006.
36. Wang, S., Lu, L., Gruetzmacher, J.A., Currier, B.L., and Yaszemski, M.J. Synthesis and characterizations of biodegradable and crosslinkable poly(epsilon-caprolactone fumarate), poly(ethylene glycol fumarate), and their amphiphilic copolymer. Biomaterials **27,** 832, 2006.
37. Peter, S.J., Miller, S.T., Zhu, G., Yasko, A.W., and Mikos, A.G. *In vivo* degradation of a poly(propylene fumarate)/beta-tricalcium phosphate injectable composite scaffold. J Biomed Mater Res **41,** 1, 1998.
38. Yaszemski, M.J., Payne, R.G., Hayes, W.C., Langer, R., and Mikos, A.G. *In vitro* degradation of a poly(propylene fumarate)-based composite material. Biomaterials **17,** 2127, 1996.
39. Jabbari, E., Wang, S., Lu, L., Gruetzmacher, J.A., Ameenuddin, S., Hefferan, T.E., Currier, B.L., Windebank, A.J., and Yaszemski, M.J. Synthesis, material properties, and biocompatibility of a novel self-cross-linkable poly(caprolactone fumarate) as an injectable tissue engineering scaffold. Biomacromolecules **6,** 2503, 2005.
40. Wang, S., Kempen, D.H., Simha, N.K., Lewis, J.L., Windebank, A.J., Yaszemski, M.J., and Lu, L. Photo-cross-linked hybrid polymer networks consisting of poly(propylene fumarate) and poly(caprolactone fumarate): controlled physical properties and regulated bone and nerve cell responses. Biomacromolecules **9,** 1229, 2008.
41. Lee, K.W., Wang, S., Lu, L., Jabbari, E., Currier, B.L., and Yaszemski, M.J. Fabrication and characterization of poly (propylene fumarate) scaffolds with controlled pore structures using 3-dimensional printing and injection molding. Tissue Eng **12,** 2801, 2006.
42. Dore-Duffy, P., Balabanov, R., Beaumont, T., Hritz, M.A., Harik, S.I., and LaManna, J.C. Endothelial activation following prolonged hypobaric hypoxia. Microvasc Res **57,** 75, 1999.
43. Mehrhof, F.B., Muller, F.U., Bergmann, M.W., Li, P., Wang, Y., Schmitz, W., Dietz, R., and von Harsdorf, R. In cardiomyocyte hypoxia, insulin-like growth factor-I-induced antiapoptotic signaling requires phosphatidylinositol-3-OH-kinase-dependent and mitogen-activated protein kinase-dependent activation of the transcription factor cAMP response element-binding protein. Circulation **104,** 2088, 2001.
44. Patrick, C.W., Jr. Adipose tissue engineering: the future of breast and soft tissue reconstruction following tumor resection. Semin Surg Oncol **19,** 302, 2000.
45. Petit, C., Pietri-Rouxel, F., Lesne, A., Leste-Lasserre, T., Mathez, D., Naviaux, R.K., Sonigo, P., Bouillaud, F., and Leibowitch, J. Oxygen consumption by cultured human cells is impaired by a nucleoside analogue cocktail that inhibits mitochondrial DNA synthesis. Mitochondrion **5,** 154, 2005.
46. Casey, T.M., and Arthur, P.G. Hibernation in noncontracting mammalian cardiomyocytes. Circulation **102,** 3124, 2000.
47. Hollister, S.J. Porous scaffold design for tissue engineering. Nat Mater **4,** 518, 2005.
48. Wake, M.C., Gupta, P.K., and Mikos, A.G. Fabrication of pliable biodegradable polymer foams to engineer soft tissues. Cell Transplant **5,** 465, 1996.
49. Lu, L., and Mikos, A.G. The importance of new processing techniques in tissue engineering. MRS Bull **21,** 28, 1996.
50. Nam, Y.S., Yoon, J.J., and Park, T.G. A novel fabrication method of macroporous biodegradable polymer scaffolds using gas foaming salt as a porogen additive. J Biomed Mater Res **53,** 1, 2000.
51. Ikada, Y. Challenges in tissue engineering. J R Soc Interface **3,** 589, 2006.
52. Hollister, S.J., Lin, C.Y., Saito, E., Schek, R.D., Taboas, J.M., Williams, J.M., Partee, B., Flanagan, C.L., Diggs, A., Wilke, E.N., Van Lenthe, G.H., Muller, R., Wirtz, T., Das, S., Feinberg, S.E., and Krebsbach, P.H. Engineering craniofacial scaffolds. Orthod Craniofac Res **8,** 162, 2005.
53. Holy, C.E., Fialkov, J.A., Davies, J.E., and Shoichet, M.S. Use of a biomimetic strategy to engineer bone. J Biomed Mater Res A **65,** 447, 2003.
54. Socha, J.J., Westneat, M.W., Harrison, J.F., Waters, J.S., and Lee, W.K. Real-time phase-contrast x-ray imaging: a new technique for the study of animal form and function. BMC Biol **5,** 6, 2007.
55. Kantor, B., Jorgensen, S.M., Lund, P.E., Chmelik, M.S., Reyes, D.A., and Ritman, E.L. Cryostatic micro-computed tomography imaging of arterial wall perfusion. Scanning **24,** 186, 2002.
56. Kasser, U., Kroemer, H., Altrock, G., and Heimburg, P. Reference ranges of viscoelasticity of human blood. Biorheology **25,** 727, 1988.
57. Kleinstreuer, C. Biofluid Dynamics: Principles and Selected Applications. Boca Raton, FL: CRC/Taylor & Francis, 2006.

Address correspondence to:
Erik L. Ritman, M.D., Ph.D.
Physiological Imaging Research Laboratory
Department of Physiology and Biomedical Engineering
Alfred 2–409
Mayo Clinic College of Medicine
200 First St. SW
Rochester, MN 55905

E-mail: elran@mayo.edu

Received: July 7, 2008
Accepted: November 25, 2008
Online Publication Date: January 15, 2009